ARTICLE

Spherical Core-Shell Alumina Support Particles for Model Platinum Catalysts

Lisa Geerts,[a] Hannelore Geerts-Claes,[a] Alexander Skorikov,[b] Julie Vermeersch,[a] Gina Vanbutsele,[a] Vladimir Galvita,[c] Denis Constales,[d] C. Vinod Chandran,[a] Sambhu Radhakrishnan,[a] Jin Won Seo,[e] Eric Breynaert,[a] Sara Bals,[b] Sreeprasanth Pulinthanathu Sree [a] and Johan A. Martens *[a]

γ- and δ-alumina are popular catalyst support materials. Using a hydrothermal synthesis method starting from aluminum nitrate and urea in diluted solution spherical core-shell particles with uniform particle size of about 1 μm were synthesized. Upon calcination at 1000 °C, the particles adopted a core-shell structure with γ-alumina core and δ-alumina shell as evidenced with 2D and 3D electron microscopy and ^{27}Al magic angle spinning nuclear magnetic resonance spectroscopy. The spherical alumina particles were loaded with Pt nanoparticles with an average size below 1 nm using strong electrostatic adsorption method. Electron microscopy and energy dispersive X-ray spectroscopy revealed a homogeneous platinum dispersion over the alumina surface. These platinum loaded alumina spheres were used as model catalyst for bifunctional catalysis. Physical mixtures of Pt/alumina spheres and spherical zeolite particles are equivalent to catalysts with platinum deposited on the zeolite itself facilitating investigation of the catalyst components individually. The spherical alumina particles are very convenient supports for obtaining a homogeneous distribution of highly dispersed platinum nanoparticles. Obtaining such small Pt particle size is challenging on other support materials such as zeolites. The here reported and well-characterized Pt/alumina spheres can be combined with any zeolite and used as a bifunctional model catalyst. This is an interesting strategy for examination of the acid catalytic function without interference of the supported platinum metal on the investigated acid material.

Introduction

Heterogeneous catalysts are generally very complex materials consisting of multiple components. Many catalysts consist of metal nanoparticles deposited on porous metal oxides.[1–3] Deriving intrinsic kinetic data from kinetic experiments on heterogeneous catalysts is complicated by the involvement of multicomponent diffusion and adsorption in the porous matrix and the presence of temperature gradients.[3–6] This complexity motivates the use of model catalysts for investigating reaction mechanisms and kinetics.[3,4] One approach consists of using single-crystal surfaces and nanoparticles on planar supports in ultra-high vacuum surface science experiments.[3,4,7,8] This approach generated important insight in catalysis, e.g.

molecular description of active sites and reaction intermediates, and it revealed structure sensitivity and promotor effects. The translation of these surface science concepts to real world fully formulated catalysts is not trivial.[8,9] Spherical support particles of which the surface can be loaded uniformly with the active metal phase may bridge between the two research fields. Examples of this type of model catalysts are Rh, Co and Ni particles on SiO_2 spheres and Pd on Al_2O_3 spheres.[10–13] Monodisperse silica particles made with the Stöber process, have been used as model catalyst support for Pt, Pd, Ag and Au nanoparticles.[14]

Alumina, especially gamma, theta and eta alumina, are used as catalyst and catalyst support, next to adsorbent, ceramic, abrasive and filter.[15–20] Many particle shapes such as rods, fibrous structures, flakes and spheres have been reported.[18,21–27] Alumina spheres can be synthesized using sol–gel processes and hydrothermal procedures, from micro-emulsion, or using spray drying, spray pyrolysis or via other ways.[22,28–36] Among the methods, precipitation is a simple, fast method suitable for upscaling.[37,38] The sphere sizes are in the range from nanometre to millimetre. The interior can be hollow, porous or dense. Only rarely documented are spheres with a core-shell architecture, with core and shell being a different alumina phase. The original alumina phase is converted upon calcination in transition alumina phases, and ultimately the fully dehydroxylated most stable α-alumina phase is obtained.[39] The transformation is

a. KU Leuven, Center for Surface Chemistry and Catalysis, Celestijnenlaan 200F, 3001 Leuven, Belgium.

b. University of Antwerp, Electron Microscopy for Materials Science, Groenenborgerlaan 171 2020 Antwerpen , Belgium.

c. Ghent University, Laboratory for Chemical Technology, Technologiepark 125, 9052, Zwijnaarde, Belgium.

d. Ghent University, Department of Electronics and information systems, Krijgslaan 281 S8, 9000, Ghent, Belgium.

e. KU Leuven, Department of Materials Engineering, Kasteelpark Arenberg 44, bus 2450, 3001 Leuven, Belgium

* johan.martens@kuleuven.be

influenced by the starting material, the particle size, relative humidity, alkalinity, heating rate, pressure and bed depth.[20]

Porous alumina spheres ranging in sizes from few hundred nanometers to few hundred micrometers have been prepared using various routes like sol-gel[28,35,40], sol-emulsion-gel[41–43], polymerization[31,44], micro-emulsion[33], hydro-solvothermal process[22,45–47], controlled hydrolysis[48], thermal decomposition of aluminum alkoxides[48], urea precipitation [16,19,27,49–53], thermal treatment of aluminium[54], spray pyrolysis[32,55–58] and synthesis in organic solvents with amphiphilic triblock copolymer etc.[59,60] Hollow spheres having a permeable shell composed of aggregated nanoplatelets/nanoparticles have been prepared using hydrothermal and solvothermal methods.[61–63] Sizes of up to a few micrometer were obtained in presence of urea and/or trisodium citrate.[15,29,62,64–67] Spray pyrolysis has been used to prepare nanosized hollow alumina nanospheres with a porous shell.[68] Hard templating is another method for synthesis of porous hollow spheres.[69–71] Sol-gel chemistry has also been applied for synthesis of hollow spheres.[72,73] In another procedure, hollow alumina spheres and solid spheres were synthesized with water in oil in water (W/O/W) emulsions.[74] In a synthesis stemming from $Al(NO_3)_3$ in water/acetone solution, by adjusting the reaction time, the properties of the obtained alumina spheres were tunable from a uniform solid to core–shell and hollow.[61]

In the present work, core-shell spherical alumina particles were synthesized via alumina precipitation with urea followed by calcination up to 1000 °C to provoke the transformation to transition alumina. The synthesis of alumina spheres with urea precipitation is challenging because pH, nature of salts and bases, and their addition sequence matter and need to be meticulously controlled.[49,51,52] Perfectly spherical alumina particles with narrow size distribution have been rarely reported, and the characterization of obtained core-shell particles remained limited. Here the presence of core-shell structures is investigated using (scanning) transmission electron microscopy and electron tomography. The transition alumina phases were identified and quantified using ^{27}Al magic angle spinning (MAS) nuclear magnetic resonance (NMR) spectroscopy.[20] Further, the core-shell alumina particles were used as support for platinum. Deposition of H_2PtCl_6 precursor by strong electrostatic adsorption on the alumina surface in acidic conditions followed by reduction with hydrogen leads to high dispersion and uniform platinum deposition. The platinum loaded core shell particles were used as hydrogenation-dehydrogenation catalyst and admixed with acid erionite zeolite agglomerate particles of similar size to prepare bifunctional catalysts. The platinum loaded core-shell alumina particles were found useful for investigating bifunctional catalysis and the positioning of Pt metal with respect to zeolite acid sites.

Materials and Methods

Preparation of the alumina spheres
All chemicals and reagents were analytical grade and used without further purification. 1.065 g aluminum nitrate $(Al(NO_3)_3.9H_2O$, Chem-Lab) was dissolved in 1000 g MilliQ water in a 1 l Schott bottle. 0.4757 g ammonium sulfate (RPL, UCB) and 6.006 g urea (Sigma-Aldrich) were sequentially added. The mixture was vigorously stirred at room temperature. When dissolution was complete, the bottle was sealed and transferred to an oven at 90 °C. The precipitation of the alumina particles was provoked by the temperature-induced decomposition of urea which increased the pH.[50,75,76] The bottle was left 24 h in the oven. After cooling to room temperature, the suspension was centrifuged and successively washed with deionized water, ethanol (technical grade) and deionized water. The wet precipitate was dried at 60 °C for 12 h. Finally, the resulting powder was calcined in air at 1000 °C for 4 h with a ramp rate of 2 °C/min.

Preparation of erionite zeolite
The erionite zeolite was synthesized according to a modified procedure reported by Lee et al.[77] The synthesis mixture was prepared using tetraethylammonium hydroxide solution (Aldrich, 35 % by weight in water), aluminum-sec-butoxide (Fluka analytical), Ludox AS-40 colloidal silica (Aldrich), hexamethoniumbromide (Sigma) and potassium chloride (Chem-Lab). The first step of the gel preparation consisted of dissolution of 0.988 g aluminum-sec-butoxide in 43.88 g tetraethylammonium hydroxide solution. 19.27 g of Ludox was subsequently added dropwise and under stirring. After homogenization, 5.82 g hexamethoniumbromide was added to the mixture, and next to it a solution of 0.8735 g potassium chloride in 29.16 g water. The gel was stirred at room temperature for 24 h. The gel was then transferred to a 120 mL stainless steel autoclave. The autoclave was placed in an oven at 100 °C and agitated by tumbling for 14 days. The solid product was recovered by centrifugation at 12,000 rpm, washed with deionized water and dried overnight at 60 °C. The zeolite powder was subjected to 2 consecutive ion exchanges in 0.5 M ammonium chloride (Chem-Lab) solution (1 g of zeolite in 100 ml solution) under reflux conditions for 4 h each. Finally, the zeolite powder was calcined at 550 °C for 8 h with heating rate of 1 °C/min to obtain the acid form. Further characterization of this zeolite is provided in supplementary information (Figure S1 and S2).

Platinum deposition
A strong electrostatic adsorption method[78,79] adapted from Zečević et al.[80] was used for Pt deposition on the alumina spheres. First, 0.5 g of the alumina powder was suspended in 152 ml of MilliQ water and stirred for 1 h. Then, a 0.1 M HCl solution was added dropwise until a pH of 2.6 was reached. An amount of $H_2PtCl_6·6H_2O$ (Aldrich) salt was dissolved in 16.9 ml MilliQ water, corresponding to 1 wt. % of Pt of the alumina support. This solution was added dropwise to the alumina suspension under stirring. After 3 h of stirring, the sample was filtered and washed with deionized water and dried at 60 °C. The sample was then reduced under hydrogen flow at 600 °C for 3.5 h with a ramp rate of 5 °C/min. For preparation of erionite zeolite containing 1 wt. % platinum, incipient wetness impregnation with $Pt(NH_3)_4Cl_2$ (Alfa Aesar) complex was performed. 0.0186 g platinum tetraamine complex was

dissolved in 0.9424 g of MilliQ water and then 0.100 g of zeolite was added to 0.0980 g of this solution. The slurry was mixed thoroughly by hand and dried overnight in an oven at 60 °C. The sample was pretreated at 400 °C (5 °C/min): first an oxidation for 1 h under oxygen flow, followed by reduction for 1 h under hydrogen flow.

Electron microscopy

High resolution scanning electron microscopy (HR-SEM) images were obtained on a Nova NanoSEM450 (FEI, Eindhoven). Using carbon tape, the powder samples were mounted on aluminum stubs and directly imaged without any further sample modification. Bright-field TEM (BF-TEM) and high-angle annular dark-field scanning TEM (HAADF-STEM) were performed using JEOL ARM200F electron microscope operated at acceleration voltage of 200 kV. Images in high-angle annular dark-field scanning TEM mode (HAADF-STEM) and energy-dispersive X-ray spectroscopy (EDX) elemental maps were acquired using a probe-corrected FEI Titan[3] operated at 300 kV and equipped with a four-quadrant EDX detector (Super-X). TEM samples were prepared by dispersing the powder in 2-propanol and placing a few drops of the solution onto the copper TEM grids covered with lacey carbon film (Pacific Grid Tech). Tomographic tilt series were acquired over a ±75° angular arrange with a 3° step interval using Fischione Model 2020 tomography sample holder. After aligning the images in the tilt series by a cross-correlation based algorithm, 3D reconstructions were obtained using expectation maximization (EM) method as implemented in ASTRA Toolbox.[81] Focused ion beam cross-sectioning was performed using FEI Helios NanoLab 650 instrument according to "lift-out" procedure after embedding the sample in a carbon matrix.

Nitrogen physisorption

N_2 physisorption isotherms were recorded on a Micromeritics TriStar 3000 instrument at liquid nitrogen temperature. The sample was pretreated at 400 °C in N_2 flow for 12 h before measurement.

X-ray diffraction

Powder X-ray diffraction was performed on a STOE STADI P Combi diffractometer with focusing Ge(111) monochromator (Cu Kα1 radiation) in transmission geometry with 140°-curved image plate position sensitive detector (IP PSD) with an internal IP PSD resolution of 0.03°.

Thermogravimetric analysis

Thermogravimetric analysis (TGA) was performed using a TA instrument Q500 under N_2 flow with a heating rate of 5 °C/min.

^{27}Al solid-state NMR

^{27}Al magic-angle spinning (MAS) NMR experiments were carried out on a Bruker 500 Avance III spectrometer operating at 11.74 T, with ^{27}Al Larmor frequency of 130.52 MHz. The alumina sample was packed in a 4 mm zirconia rotor and spun in triple-resonance 4 mm MAS probe up to a rotation frequency of 15 kHz. A radio-frequency (RF) pulse of 125 kHz strength with a flip-angle of 15 degree was used to record the ^{27}Al spectrum. ^{1}H decoupling at RF strength of 60 kHz was achieved by robust SW$_f$-SPINAL sequence.[82] 1024 transients were collected with a recycle delay of 2 s. The ^{27}Al chemical shifts were referenced against 1 M solution of aluminium nitrate (at 0 ppm). The

spectral decomposition was carried out with the help of DMFit program.[83]

Catalysis

Bifunctional catalysts were prepared by combining the zeolite powder with the Pt-loaded alumina spheres and by Pt loaded on zeolite powder diluted with inert alumina coated silica spheres. The mixing of powders was done at equal weight ratio. The catalysts are denoted as Pt-Al_2O_3/ERI and Pt-ERI/Al_2O_3. In Pt-Al_2O_3/ERI Pt is located on the alumina component, whereas in Pt-ERI/Al_2O_3, Pt is located on the zeolite. The required amount of the two powders were made into a physical mixture by combining them in a beaker using a spatula, after which the powder mixture was compressed to pellets with diameters between 125 and 250 μm. n-Decane (Acros) hydroconversion was performed in high-throughput fixed-bed continuous-flow reactor.[84,85] 50 mg of catalyst was loaded in the microreactor tubes with an internal diameter of 2 mm. The reactor was operated at a total pressure of 0.45 MPa and a molar ratio of H_2 to n-decane of 214. The space time at the reactor entrance, W/F, was 1.400 kg s mol^{-1}. Before the reaction, the catalyst was pretreated at 400 °C under hydrogen flow for 2 h. The reactor was cooled to 120 °C and n-decane/H_2 mixture admitted. The reaction temperature was increased stepwise with 5 °C. Reaction products were sampled at the reactor outlet after equilibration at a given temperature for 1 h. Reaction product analysis was achieved using an automated online GC equipped with a non-polar capillary column (HP-1, Agilent) and flame ionization detector.

Results and discussion

SEM, TEM and STEM images of the non-calcined alumina particles are shown in Figure 1. The particles had spherical morphology with typical diameters of 0.98 - 1.20 μm. Small amounts of impurities with irregular shape and elongated features were also present (Figure 1c upper left corner). Most of the particles exhibited a perfect spherical shape with a denser shell region, which can be observed in the HAADF-STEM image of an individual particle (Figure 1d). TEM and HAADF-STEM images revealed the presence of a denser shell region with thickness of about 100 nm.

To reveal the phase of the core-shell precursor particles, ^{27}Al solid-state NMR experiments were performed (Figure 2). The ^{27}Al MAS NMR spectrum exhibits three distinct signals. According to literature, the isotropic chemical shifts (δ_{iso}) in the range between 60 to 80 ppm, 30 to 50 and -20 to 20 ppm can be assigned to tetra-, penta- and hexa-coordinated Al sites, respectively. The non-calcined precursor was mainly composed of hexa-coordinated Al, typical of crystalline aluminum hydroxide and oxyhydroxide phases. The tetra- and penta-coordinated Al are characteristic of an amorphous phase.[20]
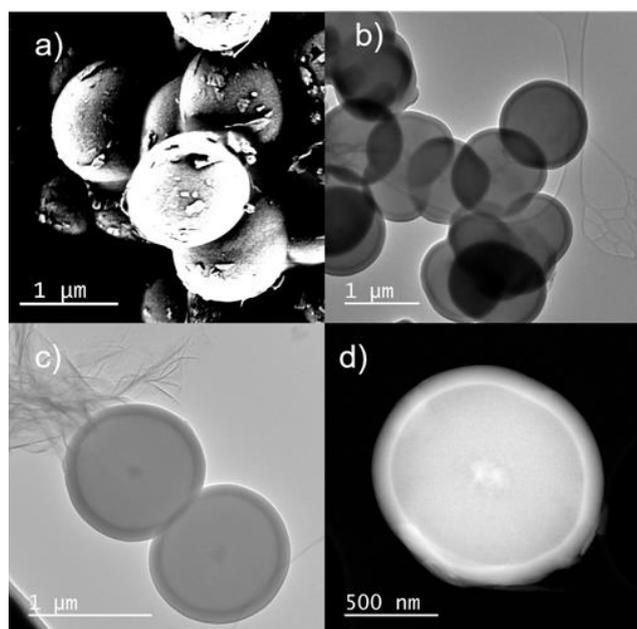
Fig. 1. Electron microscopic characterization of the precursor spheres (before calcination) a) HR-SEM b-c) TEM and d) HAADF-STEM image.

The thermal transformation was investigated by thermogravimetric analysis (Figure 3). The significant weight loss upon heating is due to dehydroxylation and elimination of residual nitrate, if any.[49] Around 950 °C, there was a step in the weight loss where after the weight remained almost constant. The total weight loss corresponded to ca. 36.5 %.

TEM and STEM revealed that despite the significant weight loss upon calcination (Figure 3), the particles showed little shrinkage upon calcination at 1000 °C (Figure 4). The size of the calcined spheres was ranging from 0.96 to 1.18 μm. The shell underwent shrinkage up to ca. 80 nm after calcination.

The internal structure of the spheres was revealed by electron tomography. The tomography experiment was performed on 2 individual particles. Figure 5 shows 2D slices and cuts through the 3D reconstructions of the particles. Movies of the 3D reconstructions can be found in the supplementary information
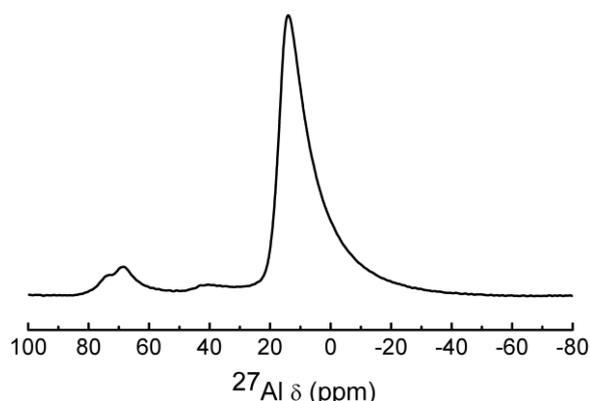

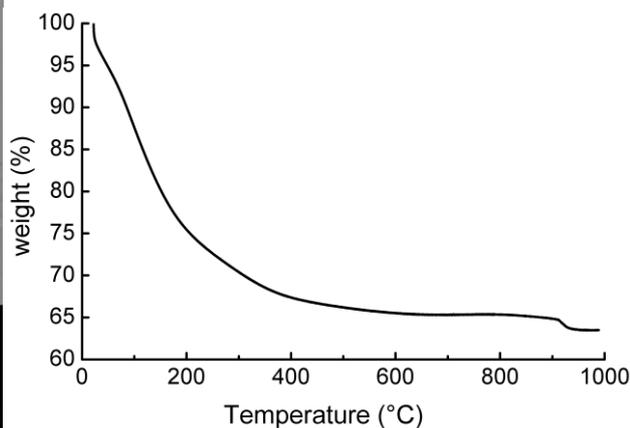**Fig. 2.** ^{27}Al MAS NMR of the uncalcined alumina precipitate.

Fig. 3. TGA curve of the precipitated Al spheres

(supplementary movie S1 and S2). Figures 5a and b show a particle with a dense shell and a less dense core, whereby the shell and core are separated by a void. In the center of the core, a denser part can be discriminated. In the 3D reconstruction of the second particle (Figure 5c and d) the void between core and shell is absent and the central dense core has a smaller size.

The nature of the transition alumina phases of the calcined core-shell particles was investigated using ^{27}Al solid-state NMR. ^{27}Al MAS and 3QMAS NMR spectra of the alumina spheres are shown in Figure 6. The 3QMAS experiment rendered high-resolution in the [27]Al spectrum. Seven different aluminum species were identified. The [27]Al spectrum shows two distinct sets of peaks centered at around chemical shifts of 12 ppm and 70 ppm corresponding to hexa- and tetra-coordinated sites, respectively.[86] The ^{27}Al NMR spectrum was decomposed using the information from the 3QMAS experiment and the fitting parameters (chemical shift δ_{iso}, quadrupolar coupling constants C_Q, asymmetry parameter η_Q and relative fractions of the
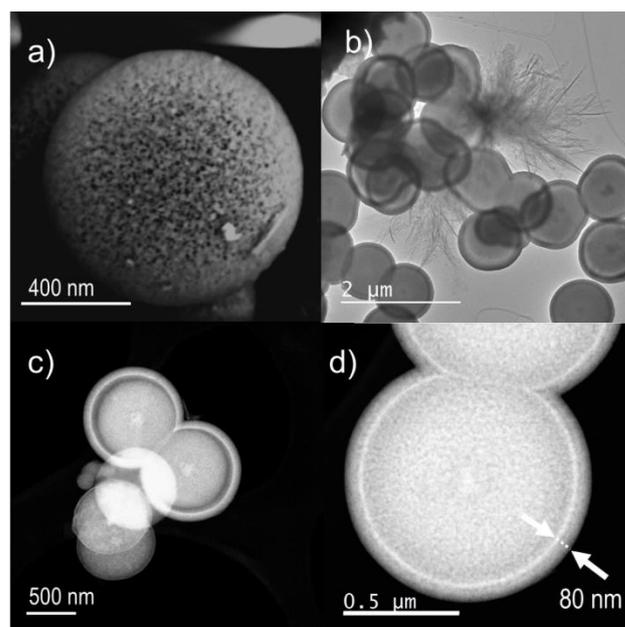

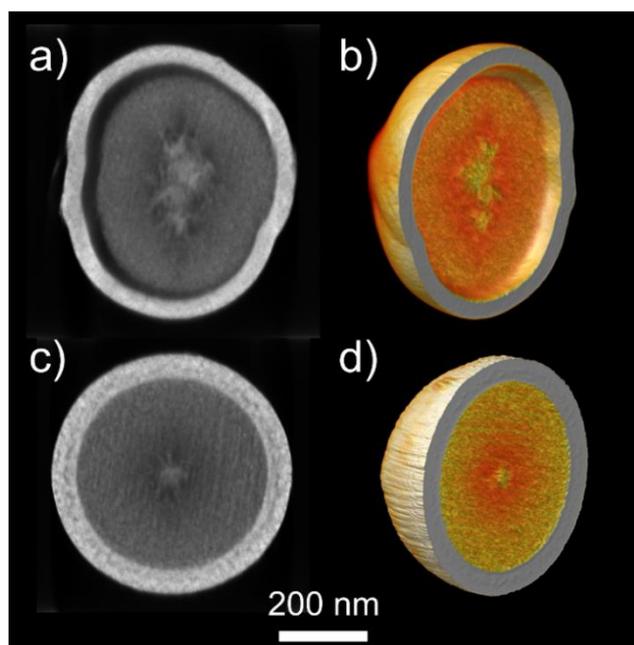**Fig. 4.** a) HR-SEM b) TEM and c-d) HAADF-STEM image of the calcined alumina spheres.

Fig. 5. a,c) Orthoslices and b,d) cuts through 3D visualizations of HAADF-STEM tomographic reconstructions of two alumina particles after calcination at 1000 °C (supplementary movies S1 and S2).

phases) are presented in Table 1. The identification of the alumina phases based on solid-state NMR parameters was carried out using the strategy published in a recent review.[20] 36 % of the calcined alumina sample is attributed to δ-alumina, 46 % to γ-alumina, and 17 % to amorphous phase. About 1 % of the alumina is present in an α-alumina phase.

The amorphous phase in the calcined sample detected with NMR was considered to be present outside of the core-shell particles. It was assumed to be present in the extraneous material observed after synthesis (Figure 4b). This leads to a composition of the core-shell particles of 55 % γ-alumina, 43 % δ-alumina, and 2 % α-alumina phase. Based on the particle diameter and the shell thickness averaged over 5 particles and measured with HAADF-STEM, volume fractions of the shell and core were estimated at 40 % and 60 %, respectively (as explained in the supporting information). From the phase composition according to NMR and the volumetric composition according to HAADF-STEM, it appears that the shell could consist of δ-alumina, and the core of γ-alumina.

The sequence of formation of transition alumina phases at increasing temperatures corresponds to γ-Al_2O_3 → δ-Al_2O_3 → θ-Al_2O_3 → α-Al_2O_3.[20] The estimated theoretical density of alumina phases increases in this order: γ-Al_2O_3 (3.2-3.65 g/cm³) → δ-Al_2O_3 (3.2 g/cm³) → θ-Al_2O_3 (3.56 g/cm³) → α-Al_2O_3 (3.98 g/cm³).[87,88] These are the densities of the bulk phases. Practical transition alumina materials are polycrystalline with a substantial amount of interstitial voids between the crystallites which are often hardly 10 nm large, leading to lower apparent densities. This is probably the case here with delta alumina phase being a more compact polycrystalline phase compared the gamma phase deeper in the particle.

The shell has the highest intensity in HAADF-STEM, in agreement with the presence of the δ-Al_2O_3, while the core is less dense and composed of γ-Al_2O_3. The α-alumina is assumed to be present as islands on the surface of the particles. The formation of α-alumina requires the highest temperature. In calcination processes, α-alumina grows from the surface towards the core of the particle.[53,86,89,90]
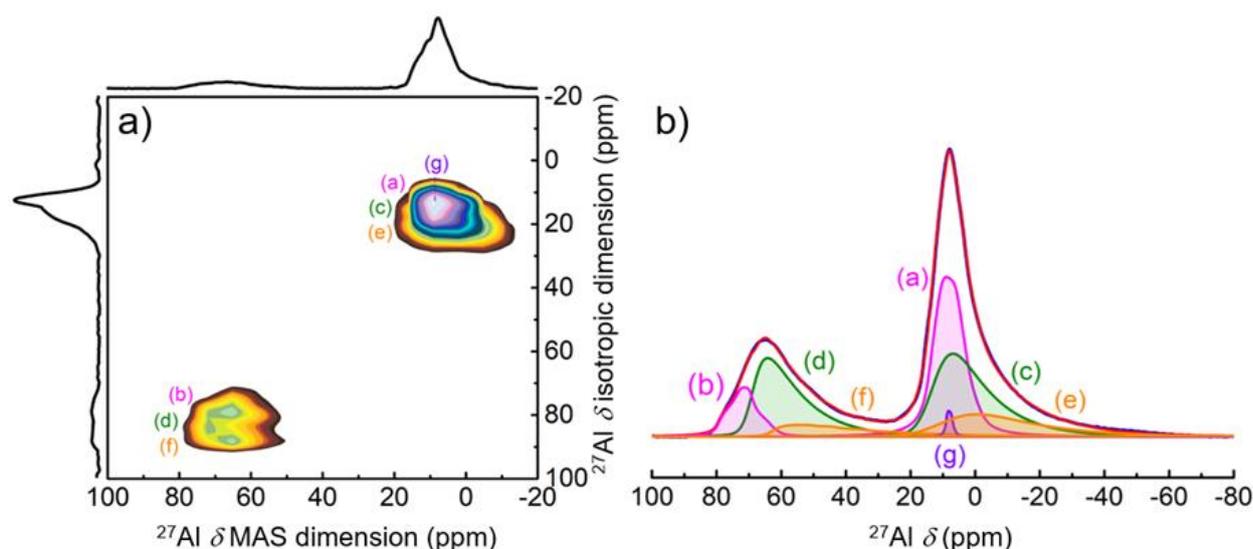

Fig. 6. a) ^{27}Al 3QMAS and b) MAS NMR of the calcined alumina spheres (1000 °C). The blue and red lines respectively correspond to the experimentally obtained and simulated spectrum. The other colors (marked a-g) show the individual simulated signals.

ARTICLE

Table 1. ^{27}Al solid-state NMR simulation parameters (chemical shift δ_{iso}, quadrupolar coupling constants C_Q and asymmetry parameter η_Q) of the alumina phases. The letters correspond to the NMR signals in Figure 6.

	C_Q (MHz)	δ_{iso} (ppm)	η_Q	Δ_{CS} (ppm)	Sites	Assignment	Content (%)
(a)	4.20	14.50	0.42	0.00	AlO_6	δ-alumina	36
(b)	4.40	79.50	0.70	0.00	AlO_4		
(c)	5.58	13.50	0.61	8.95	AlO_6	γ-alumina	46
(d)	5.42	69.40	0.61	5.30	AlO_4		
(e)	7.16	10.95	0.61	16.70	AlO_6	amorphous	17
(f)	7.90	63.30	0.61	3.50	AlO_4		
(g)	1.88	9.18	0.00	0.00	AlO_6	α-like islands on the surface	1

In our preparations we departed from aluminum hydroxide and oxyhydroxide precursor particles prepared in aqueous medium. Upon heat treatment, these precursor phases are converted to transition alumina phases, and ultimately the fully dehydroxylated α-alumina phase. Dehydroxylation and sintering lead to a loss of structural water and a volume reduction respectively. The rim of the particles will have been exposed to the highest temperatures and will have experienced the strongest sintering.

A schematic representation of the proposed composition of the core-shell alumina particles is shown in Figure 7.

The porous structure and texture of the particles were investigated with N_2 adsorption porosimetry. Nitrogen adsorption-desorption isotherms, t-plot and the corresponding pore-size distribution curves of the sample after calcination at 1000 °C are included in the supplementary information (Figure S3). The Brunauer–Emmett–Teller (BET) specific surface area

Fig. 7. Schematic arrangement of transition alumina phases in the core-shell alumina particles.

estimated by using the multipoint BET method using the adsorption data in the relative pressure range of 0.05-0.1 was 76 m^2/g. This value is too large for spherical particles measuring around 1 micrometer. The corrugated external surface observed in SEM and TEM (Figures 4 and 5) and the presence of mesopores with diameters from 6 and 20 nm and a volume of 0.12 ml/g explains the larger surface area.

The core-shell alumina particles were loaded with platinum using the strong electrostatic adsorption of chloroplatinate on the protonated surface.[78,80] Figure 8 e-f shows a typical EDX elemental map of an individual alumina sphere loaded with platinum. The distributed Pt signal indicates that Pt particles are homogeneously spread. Figure 8 a-c displays high magnification HAADF-STEM images of the Pt loaded alumina spheres. The images confirm the high dispersion with Pt particles isolated from each other and uniformly distributed on the support. The size of the Pt particles was estimated to be below 1 nm. The corresponding size histogram, estimated from 100 Pt nanoparticles on the HAADF-STEM images, is displayed in Figure 9. This size range of the Pt particles corresponds to the size of highly dispersed Pt catalysts supported on alumina used experimentally and industrially.[91–97]

To understand the extent of dispersion of Pt nanoparticles towards the interior of the alumina spheres, an approximately 100 nm thick slice of an alumina sphere was obtained using a focused ion beam (FIB), and HAADF-STEM images of this cross-section were made. The images are shown in Figure 10. The high magnification STEM images obtained from the cross-section revealed presence of particles both towards the core of the alumina spheres as on the outer surface. As shown in Figure 10,
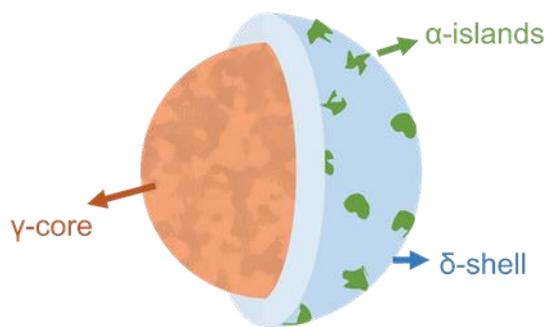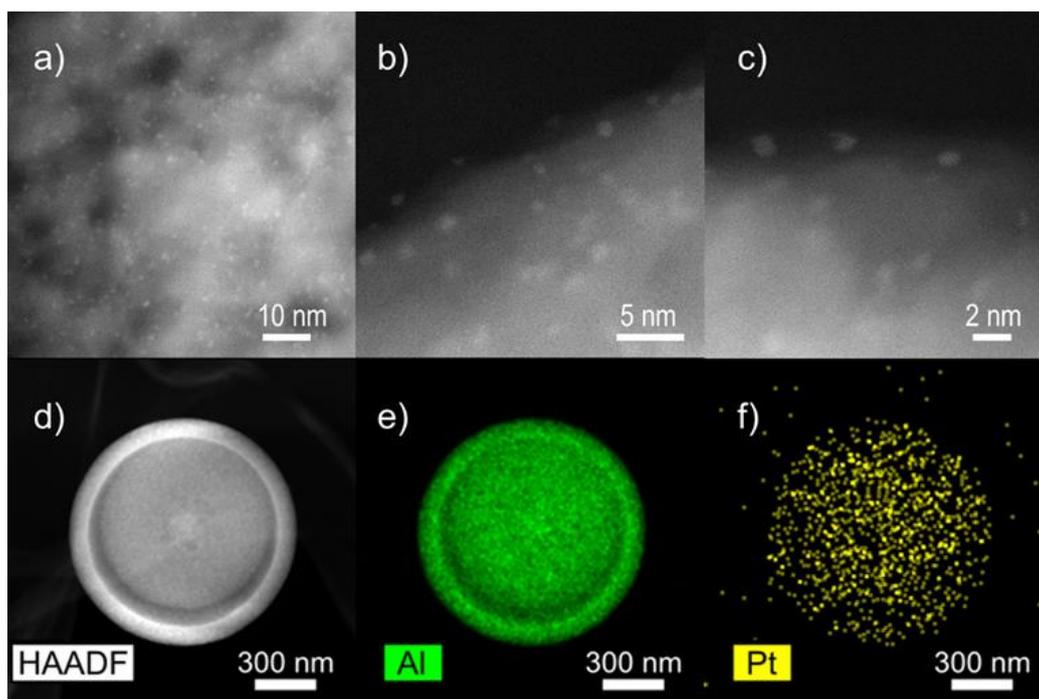
Fig. 8. a-c) High magnification HAADF-STEM images of the Pt decorated alumina spheres. d) HAADF-STEM image and EDX elemental mapping of e) Al and f) Pt on an individual alumina sphere, proving the uniform distribution of the Pt nanoparticles on the alumina support.

the Pt nanoparticles are homogeneously distributed on the alumina spheres. This is in agreement with the work of Regalbuto because both alumina phases have the same affinity towards Pt complexes.[98]

To reveal the relevance of the platinum-loaded core-shell alumina particles, the spheres were combined with powder of acid erionite zeolite with a similar spherical morphology and size (Figure 11). Such combination of a platinum catalyst with an acid zeolite can serve as bifunctional catalyst for isomerization and hydrocracking of hydrocarbons. Pt was also deposited on the ERI zeolite and mixed with inert material (alumina coated silica spheres). Figure 11 c-f shows the ERI spheres after Pt deposition. The Pt nanoparticles are homogeneously distributed and have sizes in the range from 1.6 nm to 7.7 nm.

n-Decane is a model molecule which often has been used to evaluate the bifunctional catalytic properties of zeolites.[99–103] The physical mixture of acid zeolite with Pt loaded core-shell alumina, and the zeolite loaded with platina, diluted with inert spheres were loaded in a fixed bed continuous flow reactor, having in both cases the same amount of acid zeolite and platinum.
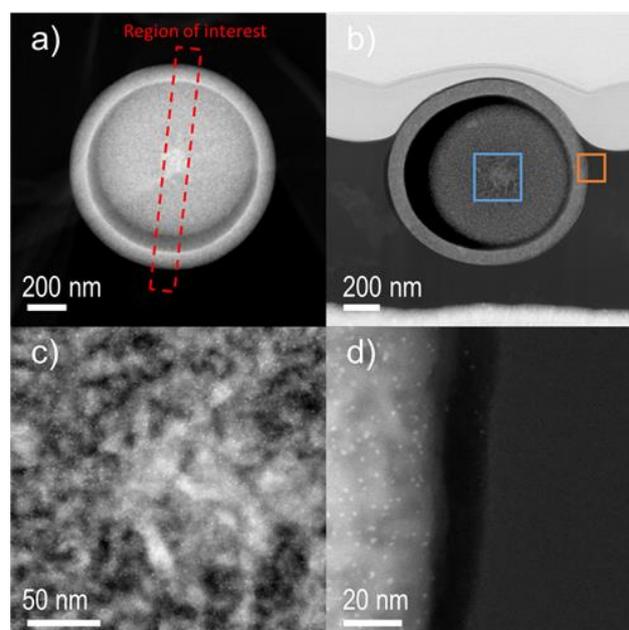

Fig. 10. HAADF-STEM images of the Pt/alumina spheres: a) image of the Pt/alumina sphere showing the region of interest for FIB cross-sectioning. b) planar view of the FIB-cross section. c and d) images zooming into the fields marked with the blue and orange squares in b.
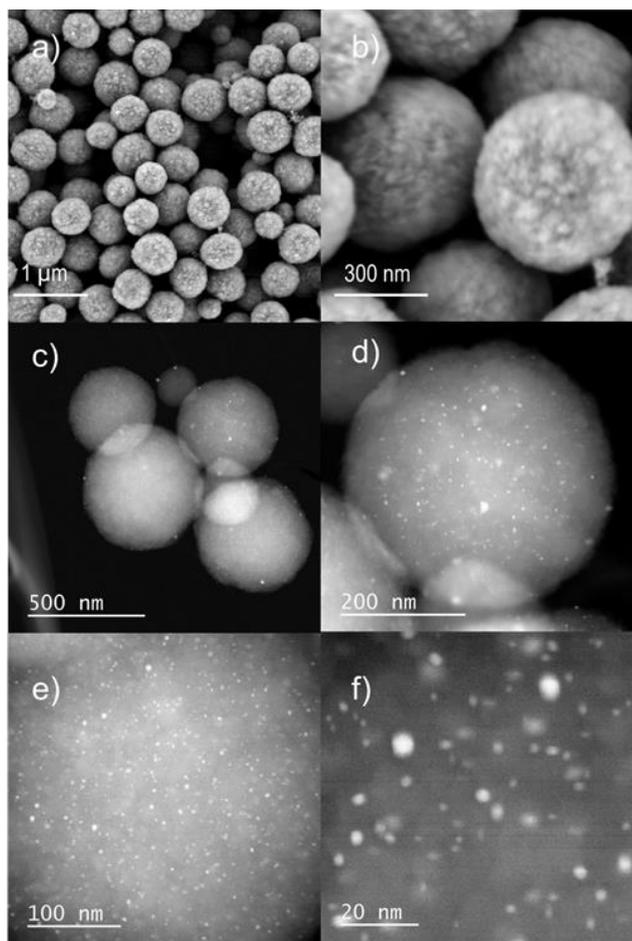
Fig. 11. a and b) Scanning electron microscopy (SEM) image of the erionite zeolite. c-f) HAADF-STEM image of the Pt loaded erionite spheres at different magnifications.

It is the zeolite particles admixed with Pt-loaded alumina spheres that provide acid sites which are active in bifunctional catalysts. The erionite zeolite was chosen because of its spherical particle morphology similar to the Pt/Al_2O_3 which facilitates homogeneous mixing of the two powders. In the mixture of Pt/Al_2O_3 and zeolite, n-decane is dehydrogenated on the metal site. The alkene diffuses to an acid site on a zeolite particle where chemisorption transforms it to an alkylcarbenium ion that undergoes skeletal rearrangement and cracking reactions. The isomerized an cracked alkylcarbenium
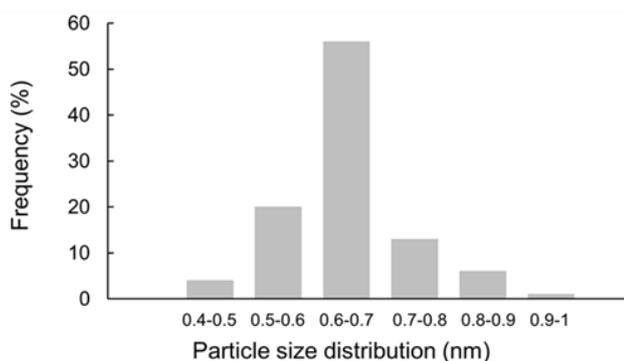

Fig 9. size histogram obtained from HAADF-STEM images of the deposited Pt nanoparticles on the alumina spheres as shown in figure 8.
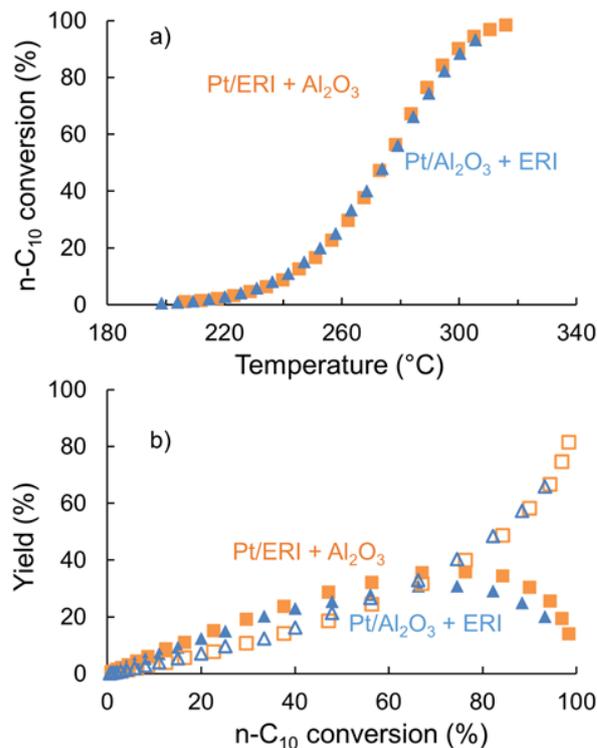

Fig. 12. a) n-decane conversion against reaction temperature on two catalysts: physical mixture of platinum-loaded core-shell alumina and acid erionite zeolite (Pt/Al_2O_3 + ERI) and platinum-loaded acid erionite zeolite diluted with Al_2O_3 spheres (Pt/ERI + Al_2O_3; b) yield of isomerization (closed symbols) and cracked products (open symbols) against n-decane conversion over both catalysts.

ions are deprotonated and desorbed from the acid sites. They diffuse and reach a platinum particle on the alumina where hydrogenation takes place.[80,100,104–106] This process overall leads to the formation of isoalkanes with 10 C-atoms referred to as feed isomers, and smaller alkanes from the cracking.

The two catalysts were equally active as the decane conversion versus reaction temperature coincided (Figure 12a). Decane is converted to branched skeletal isomers, and cracked products. Also the yield of isomers and cracked products on both catalysts were very similar. In isomerization, the maximum yield is also very little different, viz. 31 % for Pt/Al_2O_3+zeolite and 36 % for Pt/zeolite+Al_2O_3. These results reveal that the platinum-loaded core-shell alumina spheres are suitable for investigations of bifunctional catalysis. Acid zeolites can be admixed with Pt/alumina spheres and evaluated without the need of loading the platinum on the zeolite itself.

The Pt/alumina spheres were tested without mixing with a zeolite. The Pt-loaded alumina spheres were mixed with inert silica spheres to have a same volume of catalyst bed and the same amount of platinum as in the other tests. In the temperature window of interest (204 − 320 °C), mainly linear alkanes with carbon numbers from C1 to C9 were obtained. The large majority was methane. These products are typical of hydrogenolysis of the linear decane molecule on a monofunctional platinum catalyst.[99,100]

Distributions of C10 skeletal isomers obtained by n-decane isomerization are added in Figures 13 and 14. On both catalysts,
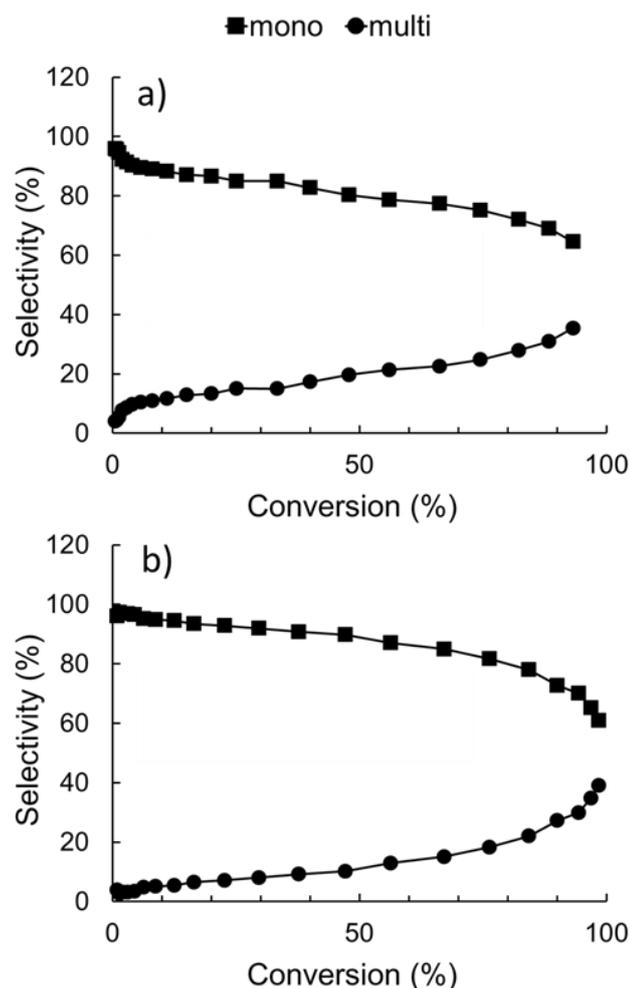
Fig. 13. Distribution of C10 skeletal isomers (mono- and multibranched) obtained by hydroconversion on a) Pt/Al$_2$O$_3$ + ERI b) Pt/ERI + Al$_2$O$_3$.

and molecular shape selectivity [99,100,105] and it has been used many times to reveal the difference between large pore zeolites with 12-membered ring windows, zeolite with large cages and 8-ring windows, and medium pore zeolites with 10-membered ring windows. These criteria were handled here to show that in the catalyst formulations with platinum on the alumina spheres or on the zeolite, the skeletal isomerization and cracking of the long alkane happen in the same molecular environment, typical of erionite zeolite having large cages and 8-membered ring windows (Table 2). The refined constraint index (CI*), which is defined as the product ratio of 2-methylnonane and 5-methylnonane at 5 % isomerization yield is 1.8 and 2.0 for Pt/Al$_2$O$_3$ + ERI and Pt/ERI + Al$_2$O$_3$, respectively.[99,101] This is in the range for cage and 8-ring zeolites. A previously investigated erionite zeolite had a CI* of 2.5.[108] Large pore zeolites have lower CI* in the range 1.0 - 2.2, and tubular 10-ring zeolites have higher CI*, up to 10.0 and more.[99–102]

The yield of ethyloctanes is also in the expected range (Table 2). The formation of branched cracked products is difficult in a zeolite with small windows such as erionite. The yield of isopentane among the cracked products is a sensitive criterion to probe the width of the pores.[99,100] On the two formulations, little isopentane is formed (Table 2). In large pore zeolites, more than 35 mol/100 mol cracked n-C10 is obtained.[109] The selectivity of the n-decane conversion confirms that irrespective of the location of platinum, the skeletal isomerization and the cracking occurs on the erionite zeolite.

the monobranched isomers were the primary reaction products (Figure 13). Di- and tribranched isomers are formed consecutive to monobranched products. The content of tribranched isomers in the fraction of multibranched isomers was below 0.6 % and was reached at the highest n-decane conversion. This sequential formation of branchings can be explained by the skeletal isomerization mechanisms of alkylcarbenium ions obtained by protonation of C10 alkenes on the acid sites of the zeolite.[99,100,105,107] Although the differences are minor, on the Pt/Al$_2$O$_3$ + ERI catalyst the introduction of a second branching is slightly faster than on the Pt/ERI + Al$_2$O$_3$ catalyst. This can be interpreted as a shorter lifetime of the monobranched alkylcarbenium ions on the acid sites by stronger chemisorption competition with other alkenes.

The evolution of the distribution of the methylnonane isomers with n-decane conversion (Figure 14) was also similar on the two catalysts. There is little change with conversion. Among the methylnonane skeletal isomers, 3-methylnonane slightly dominates, followed by 4-methylnonane and 2-methylnonane. 5-methylnonane is formed in smaller quantity. It is thermodynamically the less favored isomer.[99,100,107]

The selectivity of n-decane hydroisomerization and hydrocracking is sensitive to the pore architecture of the zeolite
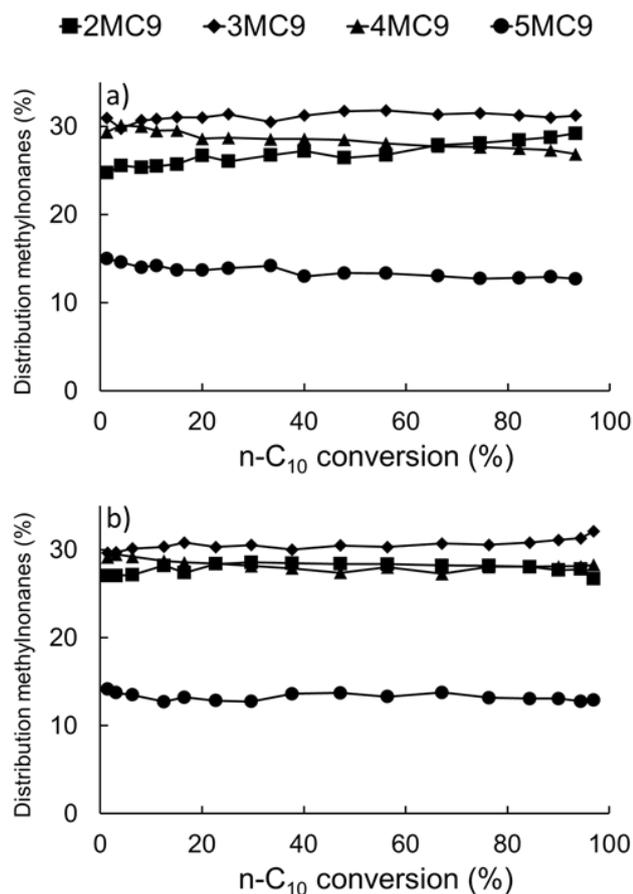
Fig. 14. Distribution of methylnonane skeletal isomers obtained on a) Pt/Al$_2$O$_3$ + ERI b) Pt/ERI + Al$_2$O$_3$.

In a previous publication, we showed that the positioning of the platinum with respect to the zeolite acid sites matters to the

catalytic activity and selectivity for isomerization versus cracking especially for n-alkanes longer than n-C10, and especially with n-C19.[80] Smaller alkanes and alkenes diffuse faster than long ones, and faster diffusivity makes the intimacy of platinum and acid sites less critical. The erionite is less active than the ultrastable Y zeolite as discussed in the previous publication.[80] This too makes the intimacy less critical. The choice of erionite in this work was motivated because of the similarity in morphology and size of the zeolite and the alumina particles and the convenience of mixing the powders. Here we provide a proof-of-concept of a convenient monofunctional platinum catalyst that can be mixed with monofunctional acid zeolites for investigating bifunctional catalysis. Extending this concept to more active acid zeolites like USY and longer n-alkanes is planned for the future, where it is expected to show the intimacy effects as previously reported.[80]

The Pt alumina spheres can be combined in various mixing ratios with many zeolites of interest. This offers a lot of flexibility for varying the acid function and the Pt metal function independently from each other, and to vary their intimacy.[80] Variations of the ratio and proximity of the metal and acid sites, of the zeolite pore structure and morphology can be systematically evaluated. Such studies will further benefit the understanding of the bifunctional mechanism.

Table 2. Reaction product criteria from n-decane hydroisomerization and hydrocracking probing pore architecture.[99,100]

	Pt/Al$_2$O$_3$ + ERI	Pt/ERI + Al$_2$O$_3$	Assignment
CI* 2MC9/5MC9 at 5 % isomerization	1.8	2	12-MR or 8 MR + cage
% ethyloctanes in monobranched isomers at 5 % isomerization	7.8	4.6	12-MR pore or 8 MR + cage
isopentane (mol/100 mol C10 cracked) at 35 % cracking	15	12	10 MR or 8 MR + cage

Conclusions

Spherical 1 μm sized core-shell alumina particles with a narrow size distribution were synthesized by the urea based precipitation method. Electron microscopy and tomography reconstruction were used to characterize the core-shell nanostructure of the calcined particles and to locate the

transition alumina phases quantified with ^{27}Al NMR spectroscopy. The particles have δ-alumina shell with small islands of α-alumina, and γ-alumina core. This organization reflects the temperatures that were reached in the calcination process, being higher outside than inside. Homogeneous loading of uniformly sized Pt nanoparticles on the alumina core-shell particles was obtained by strong electrostatic interaction of chloroplatinate precursor with the protonated surface of the

particles. The excellent accessibility of the Pt particles was confirmed in bifunctional catalysis experiments; in the isomerization and hydrocracking of n-decane a same catalytic performance was obtained with platinum on alumina spheres admixed with acid zeolite and acid zeolite loaded with platinum itself.

In bifunctional catalysis research, researchers load the acidic material itself with platinum metal and make kinetic studies. However sometimes it is difficult to obtain a good platinum distribution, and then the metal function may not function properly. What we demonstrate here is that the mixing of Pt/alumina with zeolite is a convenient way to prepare bifunctional catalysts with full control over the metal function because it is prepared independently. One can compare many acidic materials, zeolites, supported heteropolyacids, silica-alumina, and so on without modification and keeping the hydrogenation-dehydrogenation activity constant. In addition, the physical separation of the two catalyst functions is a way to control the intimacy, which is an essential feature in bifunctional catalysis.[80] In recent work colleagues have incorporated Pt particles in hollow zeolite crystals for similar purposes.[110] It reveals the potential of the core-shell alumina spheres to serve as model catalyst support.

Conflicts of interest

There are no conflicts to declare.

Author contribution statement

L. Geerts and J. Martens designed the research. L. Geerts performed material synthesis, performed (S)TEM and EDX characterization, analyzed the data and wrote the article. J. Vermeersch assisted with the material synthesis. STEM, electron tomography and EDX was done by A. Skorikov. S. P. Sree performed SEM characterization. The hydroisomerization experiments were done by G. Vanbutsele and J. Vermeersch. NMR was done by C. Vinod Chandran. All of the authors contributed to the finalization of the article. J. Martens helped with data interpretation and writing.

Acknowledgements

Notes and references

1   M. Bäumer, J. Libuda, K. M. Neyman, N. Rösch, G. Rupprechter and H. J. Freund, *Phys. Chem. Chem. Phys.*, 2007, **9**, 3541–3558.

2   F. Zaera, in *Encyclopedia of Inorganic and Bioinorganic Chemistry*, John Wiley & Sons, Ltd., 2014.

3   J. Libuda, S. Schauermann, M. Laurin, T. Schalow and H. J. Freund, *Monatshefte fur Chemie*, 2005, **136**, 59–75.

4   B. C. Gates, *Top. Catal.*, 2001, **14**, 173–180.

5   C. Chizallet and P. Raybaud, *Catal. Sci. Technol.*, 2014, **4**, 2797–2813.

6   J. Hoffmann, I. Meusel, J. Hartmann and J. Libuda, *J. Catal.*, 2001, **204**, 378–392.

7   M. Boudart, *Top. Catal.*, 2000, **13**, 147–149.

8   D. W. Goodman, *Surf. Sci.*, 1994, **299/300**, 837–848.

9   F. C. Meunier, *ACS Nano*, 2008, **2**, 2441–2444.

10   P. L. J. Gunter, J. W. H. Niemantsverdriet, F. H. Ribeiro and G. A. Somorjai, *Catal. Rev.*, 1997, **39**, 77–168.

11   C. K. Ling, N. A. M. Zabidi and C. Mohan, *J. Appl. Sci.*, 2011, **11**, 1436–1440.

12   B. A. T. Mehrabadi, S. Eskandari, U. Khan, R. D. White and J. R. Regalbuto, *A Review of Preparation Methods for Supported Metal Catalysts*, Elsevier Inc., 1st edn., 2017, vol. 61.

13   S. Chenna, R. Banerjee and P. A. Crozier, *ChemCatChem*, 2011, **3**, 1051–1059.

14   H. Hofmeister, P. Miclea, M. Steen and W. Mo, *Top. Catal.*, 2007, **46**, 11–21.

15   W. Cai, J. Yu and S. Mann, *Microporous Mesoporous Mater.*, 2009, **122**, 42–47.

16   X. J. Xu, X. D. Sun, Y. Q. Liang and W. Qiu, *Appl. Mech. Mater.*, 2013, **341**–**342**, 100–104.

17   W. Yang, H. Wang, X. Cheng, Z. Xie and L. An, *J. Am. Ceram. Soc.*, 2008, **91**, 2732–2735.

18   Y. Xie, D. Kocaefe, Y. Kocaefe, J. Cheng and W. Liu, *Nanoscale Res. Lett.*, , DOI:10.1186/s11671-016-1472-z.

19   J. Kong, B. Chao, T. Wang and Y. Yan, *Powder Technol.*, 2012, **229**, 7–16.

20   C. V. Chandran, C. E. A. Kirschhock, S. Radhakrishnan, F. Taulelle, J. A. Martens and E. Breynaert, *Chem. Soc. Rev.*, 2019, **48**, 134–156.

21   C. Bousquet, F. Cansell, C. Elissalde, M. Maglione and C. Aymonier, in *Mater. of 11th European Meeting on Supercritical Fluids: Reactions, Materials and Natural Products Processing*, 2008.

22   R. R. Manesh, M. Kohnehpoushi, M. Eskandari, Z. Fakhroueian and B. A. Nejand, *Mater. Res. Express*, 2017, **4**, 095025.

23   S. Liu, R. J. Wehmschulte and C. M. Burba, *J. Mater. Chem.*, 2003, **13**, 3107–3111.

24   V. Piriyawong, V. Thongpool, P. Asanithi and P. Limsuwan, *J. Nanomater.*, , DOI:10.1155/2012/819403.

25   C. B. Reid, J. S. Forrester, H. J. Goodshaw, E. H. Kisi and G. J. Suaning, *Ceram. Int.*, 2008, **34**, 1551–1556.

26   M. Shojaie-Bahaabad and E. Taheri-Nassaj, *Mater. Lett.*, 2008, **62**, 3364–3366.

27   H. I. Ul, K. Akhtar and Z. U. Khan, *High. Temp. Mater. Proc.*, 2015, **34**, 325–332.

28   N. Dilsiz and G. Akovali, *Mater. Sci. Eng.*, 2002, **332**, 91–96.

29   J. Zhou, L. Wang, Z. Zhang and J. Yu, *J. Colloid Interface Sci.*, 2013, **394**, 509–514.

30   R. Brace and E. Matijevic, *J. inorg. nucl. Chem.*, 1973, **35**, 3691–3705.

31   F. Liu, X. Zheng, J. Chen and L. Jiang, *RSC Adv.*, 2015, **5**, 93917–93925.

32   S. Arita, N. Aoyagi, K. Ohshita, Y. Tsubota and T. Ogihara, *J. Ceram. Soc. Japan*, 2017, **125**, 539–542.

33   Q. Chang, X. Wang, J. Zhou and Y. Wang, *Adv. Mater. Res.*, 2012, **412**, 199–202.

34   P. Liu, J. Feng, X. Zhang, Y. Lin, D. G. Evans and D. Li, *J. Phys. Chem. Solids*, 2008, **69**, 799–804.

35   A. Islam and Y. Hui, *J. Porous Mater.*, 2012, **19**, 807–817.

36   S. Cottrino, Y. Jorand, J. Adrien and C. Olagnon, *Powder Technol.*, 2013, **237**, 586–593.

37   L. Wang and N. Zhang, *Adv. Mater. Res.*, 2014, **1079**–**1080**, 62–65.

38   S. A. Hassanzadeh-Tabrizi and E. Taheri-Nassaj, *Mater. Lett.*, 2009, **63**, 2274–2276.

39   C. Pecharromán, I. Sobrados, J. E. Iglesias, T. González-Carreño and J. Sanz, *J. Phys. Chem. B*, 1999, **103**, 6160–6170.

40   H. V. Fajardo, A. O. Martins, R. M. De Almeida, L. K. Noda, L. F. D. Probst, N. L. V. Carreño and A. Valentini, *Mater. Lett.*, 2005, **59**, 3963–3967.

41   M. Chatterjee, M. K. Naskar, B. Siladitya and D. Ganguli, *J. Mater. Res.*, 2000, **15**, 176–185.

42   M. Rajendran and A. K. Bhattacharya, *Mater. Sci. Eng.*, 1999, **60**, 217–222.

43   H. Yang, Y. Xie, G. Hao, W. Cai and X. Guo, *New J. Chem.*, 2016, **40**, 589–595.

44   Q. Fu, T. He, Y. Chai and C. Liu, *J. Nat. Gas Chem.*, 2010, **19**, 557–559.

45   H. Liu, G. Lu, Y. Guo, Y. Wang and Y. Guo, *Cent. Eur. J. Chem.*, 2009, **7**, 794–802.

46   X. Song, P. Yang, C. Jia, L. Chen and K. Matras-Postolek, *RSC Adv.*, 2015, **5**, 33155–33162.

47   I. Saptiama, Y. V. Kaneti, Y. Suzuki, K. Tsuchiya, N. Fukumitsu, T. Sakae, J. Kim, Y. M. Kang, K. Ariga and Y. Yamauchi, *Small*, 2018, **14**, 1–14.

48   T. Ogihara, H. Nakajima, T. Yanagawa, N. Ogata, K. Yoshida and N. Matsushita, *J. Am. Ceram. Soc.*, 1991, **74**, 2263–2269.

49   H. S. Potdar, K. Jun, J. W. Bae, S. Kim and Y. Lee, *Appl. Cataly*, 2007, **321**, 109–116.

50   J. W. Geus and R. J. Stol, *J. Colloid Interface Sci.*, 1975, **51**, 449–458.

51   W. Zhou, S. Xiangqian and J. Maoxiang, *Adv. Mater. Res.*, 2014, **936**, 145–148.

52   K. Ada, Y. Sarıkaya and T. Alemdarog, *Ceram. Int.*, 2003, **29**, 513–518.

53   D. S. Tucker, *J. Am. Ceram. Soc.*, 1985, **68**, 163–164.

54   S. Iijima, *Jpn. J. Appl. Phys.*, 1984, **23**, L347–L350.

55   M. I. Martín, L. S. Gómez, O. Milosevic and M. E. Rabanal, *Ceram. Int.*, 2010, **36**, 767–772.

56   M. I. Martín, M. E. Rabanal, L. S. Gómez, J. M. Torralba and O. Milosevic, *J. Eur. Ceram. Soc.*, 2008, **28**, 2487–2494.

57   J. H. Kim, K. Y. Jung, K. Y. Park and S. B. Cho, *Microporous Mesoporous Mater.*, 2010, **128**, 85–90.

58   J. H. Kim, K. Y. Jung and K. Y. Park, *J. Ind. Eng. Chem.*, 2012, **18**, 344–348.

59   L. Qian, L. Li, X. Zhi-yuan and Z. Dong-yuan, *Chem. Res. Chinese Univ.*, 2001, **17**, 143–147.

60   C. Boissière, L. Nicole, C. Gervais, F. Babonneau, M. Antonietti, H. Amenitsch, C. Sanchez and D. Grosso, *Chem. Mater*, 2006, **18**, 5238–5243.

61   L. Zhang, W. Lu, R. Cui and S. Shen, *Mater. Res. Bull.*, 2010, **45**, 429–436.

62   W. Cai, S. Chen, J. Yu, Y. Hu, C. Dang and S. Ma, *Mater. Chem. Phys.*, 2013, **138**, 167–173.

63   G. Xue, X. Huang, N. Zhao, F. Xiao and W. Wei, *RSC Adv.*, 2015, **5**, 13385–13391.

64   X. Wu, B. Zhang, D. Wang and Z. Hu, *Mater. Lett.*, 2012, **70**, 128–131.

65   X. Wu, D. Wang, Z. Hu and G. Gu, *Mater. Chem. Phys.*, 2008, **109**, 560–564.

66   L. Nie, A. Meng, J. Yu and M. Jaroniec, *Sci. Reports - Nat.*, 2013, **3**, 3215.

67   W. Cai, J. Yu, B. Cheng, B. L. Su and M. Jaroniec, *J. Phys. Chem. C*, 2009, **113**, 14739–14746.

68   Y. Hu, H. Ding and C. Li, *Particuology*, 2011, **9**, 528–532.

69   J. Tian, P. Tian, H. Pang, G. Ning, R. F. Bogale, H. Cheng and S. Shen, *Microporous Mesoporous Mater.*, 2016, **223**, 27–34.

70   J. Tian, P. Tian, H. Pang and G. Ning, *Mater. Lett.*, 2018, **210**, 35–38.

71   Y. Wang and W. J. Tseng, *J. Am. Ceram. Soc.*, 2009, **92**, 32–37.

72   M. Chatterjee, D. Enkhtuvshin, B. Siladitya and D. Ganguli, *J. Mater. Sci.*, 1998, **33**, 4937–4942.

73   H. Wang, F. Wang, Q. Liao and X. Li, *Ceram. Int.*, 2015, **41**, 4959–4965.

74   L. M. Zhang, L. Han, H. Zhang, S. S. Shen and W. C. Lu, *Appl. Mech. Mater.*, 2011, **110**–**116**, 997–1002.

75   X. Jin, Q. Qi, W. Ye, Z. Feng, C. Yan-bin, L. Jie and L. Ye-xiang, *J. Cent. South Univ. Technol.*, 2007, **14**, 773–778.

76   L. Yan-hui, P. Cheng, Z. Wei, B. Ming-Min and R. Ping-Gen, *J. Inorg. Mater.*, 2014, **29**, 1115–1120.

77   J. H. Lee, M. B. Park, J. K. Lee, H. Min and M. K. Song, *J. Am. Chem. Soc.*, 2010, **132**, 12971–12982.

78   H. Cho and J. R. Regalbuto, *Catal. Today*, 2015, **246**, 143–153.

79   B. A. T. Mehrabadi, S. Eskandari, U. Khan, R. D. White and J. R. Regalbuto, in *Advances in Catalysis*, Elsevier Inc., 1st edn., 2017, vol. 61, pp. 1–35.

80   J. Zecevic, G. Vanbutsele, K. P. de Jong and J. A. Martens, *Nature*, 2015, **528**, 245–248.

81   W. van Aarle, W. J. Palenstijn, J. De Beenhouwer, T. Altantzis, S. Bals, K. J. Batenburg and J. Sijbers, *Ultramicroscopy*, 2015, **157**, 35–47.

82   C. V. Chandran and T. Bräuniger, *J. Magn. Reson.*, 2009, **200**, 226–232.

83   D. Massiot, F. Fayon, M. Capron, I. King, S. Le Calvé, B. Alonso, J. O. Durand, B. Bujoli, Z. Gan and G. Hoatson, *Magn. Reson. Chem.*, 2002, **40**, 70–76.

84   G. Burnens, C. Bouchy, E. Guillon and J. A. Martens, *J. Catal.*, 2011, **282**, 145–154.

85   W. Huybrechts, P. A. Jacobs and J. A. Martens, *Appl. Catal. A Gen.*, 2003, **243**, 1–13.

86   A. Düvel, E. Romanova, M. Shari, D. Freude, M. Wark, P.

Heitjans and M. Wilkening, *J. Phys. Chem. C*, 2011, **115**, 22770–22780.

87   H. C. Newsome, J.W., Heiser, H.W., Russel, A.S., Stumpf, *Tech. Pap. No. 10*, 1960, 89.

88   E. Yalamaç, A. Trapani and S. Akkurt, *Eng. Sci. Technol. an Int. J.*, 2014, **17**, 2–7.

89   B. Béguin, E. Garbowski and M. Primet, *Appl. Catal.*, 1991, **75**, 119–132.

90   P. Burtin, J. P. Brunelle, M. Pijolat and M. Soustelle, *Appl. Catal.*, 1987, **34**, 225–238.

91   J. H. Kang, L. D. Menard, R. G. Nuzzo and A. I. Frenkel, *J. Am. Chem. Soc.*, 2006, **128**, 12068–12069.

92   J. Singh, R. C. Nelson, B. C. Vicente, S. L. Scott and J. A. van Bokhoven, *Phys. Chem. Chem. Phys.*, 2010, **12**, 5668–5677.

93   E. Yoo, T. Okata, T. Akita, M. Kohyama, J. Nakamura and I. Honma, *Nano Lett.*, 2009, **9**, 2255–2259.

94   C. Shakthivel, L. Keerthana and I. Prabha, *Johnson Matthey Technol. Rev.*, 2019, **63**, 122–133.

95   J. G. Irwin and R. L. Moss, *J. Chem. Technol. Biotechnol.*, 1980, **30**, 657–666.

96   L. Spenadel and M. Boudart, *J. Phys. Chem.*, 1960, **64**, 204–207.

97   A. Gholidoust, A. Naderifar, M. Rahmani and S. Sahebdelfar, *Int. J. Mod. Phys. Conf. Ser.*, 2012, **05**, 168–176.

98   J. R. Regalbuto, A. Navada, S. Shadid, M. L. Bricker and Q. Chen, *J. Catal.*, 1999, **184**, 335–348.

99   J. A. Martens, M. Tielen, P. A. Jacobs and J. Weitkamp, *Zeolites*, 1984, **4**, 98–107.

100   J. A. Martens and P. A. Jacobs, *Zeolites*, 1986, **6**, 334–348.

101   W. Souverijns, L. Rombouts, J. A. Martens and P. A. Jacobs, *Microporous Mater.*, 1995, **4**, 123–130.

102   W. Souverijns, W. Verrelst, G. Vanbutsele, J. A. Martens and P. A. Jacobs, *J. Chem. Soc., Chem. Commun.*, 1994, 1671–1672.

103   C. Zschiesche, D. Himsl, R. Rakoczy, A. Reitzmann, J. Freiding, N. Wilde and R. Gläser, *Chem. Eng. Technol.*, 2018, **41**, 199–204.

104   J. E. Samad, J. Blanchard, C. Sayag, C. Louis and J. R. Regalbuto, *J. Catal.*, 2016, **342**, 213–225.

105   J. A. Martens, R. Parton, L. Uytterhoeven, P. A. Jacobs and G. F. Froment, *Appl. Catal.*, 1991, **76**, 95–116.

106   L. Geerts, R. K. Ramachandran, J. Dendooven, S. Radhakrishnan, J. W. Seo, C. Detavernier, J. Martens and S. P. Sree, *Catal. Sci. Technol.*, 2020, **10**, 1778–1788.

107   E. Verheyen, C. Jo, M. Kurttepeli, G. Vanbutsele, E. Gobechiya, T. I. Korányi, S. Bals, G. Van Tendeloo, R. Ryoo, C. E. A. Kirschhock and J. A. Martens, *J. Catal.*, 2013, **300**, 70–80.

108   P. A. Jacobs and J. A. Martens, *Pure Appl. Chem.*, 1986, **58**, 1329–1338.

109   J. A. Martens, E. Benazzi, J. Brendlé, S. Lacombe and R. Le Dred, *Stud. Surf. Sci. Catal.*, 2000, **130**, 293–298.

110   C. Dai, A. Zhang, C. Song and X. Guo, *Adv. Catal.*, 2018, **63**, 75–115.